Spin-orbit interaction in InSb nanowires

I. van Weperen,[1] B. Tarasinski,[2] D. Eeltink,[1] V. S. Pribiag,[1,*] S. R. Plissard,[1,3,†] E. P. A. M. Bakkers,[1,3]
L. P. Kouwenhoven,[1] and M. Wimmer[1,‡]

[1]*QuTech and Kavli Institute of Nanoscience, Delft University of Technology, 2600 GA Delft, The Netherlands*
[2]*Instituut-Lorentz, Universiteit Leiden, P.O. Box 9506, 2300 RA Leiden, The Netherlands*
[3]*Department of Applied Physics, Eindhoven University of Technology, 5600 MB Eindhoven, The Netherlands*

We use magnetoconductance measurements in dual-gated InSb nanowire devices, together with a theoretical analysis of weak antilocalization, to accurately extract spin-orbit strength. In particular, we show that magnetoconductance in our three-dimensional wires is very different compared to wires in two-dimensional electron gases. We obtain a large Rashba spin-orbit strength of 0.5–1 eV Å corresponding to a spin-orbit energy of 0.25–1 meV. These values underline the potential of InSb nanowires in the study of Majorana fermions in hybrid semiconductor-superconductor devices.

PACS number(s): 73.20.Fz, 73.63.−b, 71.70.Ej, 03.65.Vf

Hybrid semiconductor nanowire-superconductor devices are a promising platform for the study of topological superconductivity [1]. Such devices can host Majorana fermions [2,3], bound states with non-Abelian exchange statistics. The realization of a stable topological state requires an energy gap that exceeds the temperature at which experiments are performed (∼50 mK). The strength of the spin-orbit interaction (SOI) is the main parameter that determines the size of this topological gap [4] and thus the potential of these devices for the study of Majorana fermions. The identification of nanowire devices with a strong SOI is therefore essential. This entails both performing measurements on a suitable material and device geometry as well as establishing theory to extract the SOI strength.

InSb nanowires are a natural candidate to create devices with a strong SOI, since bulk InSb has a strong SOI [5,6]. Nanowires have been used in several experiments that showed the first signatures of Majorana fermions [7–10]. Nanowires are either fabricated by etching out wires in planar heterostructures or are grown bottom up. The strong confinement in the growth direction makes etched wires two dimensional (2D) even at high density. SOI has been studied in 2D InSb wires [11] and in planar InSb heterostructures [12], from which a SOI due to structural inversion asymmetry [13], a Rashba SOI α_R of 0.03 eV Å has been obtained [12]. Bottom-up grown nanowires are three dimensional (3D) when the Fermi wavelength is smaller than the wire diameter. In InSb wires of this type, SOI has been studied by performing spectroscopy on quantum dots [14,15], giving $\alpha_R = 0.16$–0.22 eV Å [15]. However, many (proposed) topological nanowires devices [16–18] contain extended conducting regions, i.e., conductive regions along the nanowire much longer than the nanowire diameter. The SOI strength in these extended regions has not yet been determined. It is likely different from that in quantum dots, as the difference in confinement between both geometries results in a different effective electric field and thus a different Rashba SOI. Measurements of SOI strength in extended InSb nanowire regions are therefore needed to evaluate their potential for topological devices. Having chosen a nanowire material, further enhancement of Rashba SOI strength can be realized by choosing a device geometry that enhances the structural inversion asymmetry [19,20]. Our approach is to use a high-k dielectric in combination with a top gate that covers the InSb nanowire.

The standard method to extract SOI strength in extended regions is through low-field magnetoconductance (MC) measurements [21,22]. Quantum interference (see Fig. 1) in the presence of a strong SOI results in an increased conductance, called weak antilocalization (WAL) [23], that reduces to its classical value when a magnetic field is applied [24]. From fits of MC data to theory a spin relaxation length is extracted. If spin relaxation results from inversion asymmetry, a spin precession length and SOI strength can be defined. To extract SOI strength in nanowires the theory should contain (1) the length over which the electron dephases in the presence of a magnetic field, the magnetic dephasing length [25], and (2) the relation between spin relaxation and spin precession length [26]. The magnetic dephasing and spin relaxation length depend on, besides magnetic field and SOI strength, respectively, dimensionality and confinement. For instance, in nanowires, the spin relaxation length increases when the wire diameter is smaller than the spin precession length [26–28]. Therefore, the spin relaxation length extracted from WAL is not a direct measure of SOI strength. These effects have been studied in 2D wires [25,26], but results for 3D wires are lacking. As geometry and dimensionality are different (see Fig. 1), using 2D results for 3D wires is unreliable. Thus, a theory for 3D wires has to be developed.

In this Rapid Communication, we first theoretically study both magnetic dephasing and spin relaxation due to a Rashba SOI in 3D hexagonal nanowires. We then use this theory to determine the spin-orbit strength from our measurements of WAL in dual-gate InSb nanowire devices, finding a strong Rashba SOI $\alpha_R = 0.5$–1 eV Å.

―――――――――

*Present address: School of Physics and Astronomy, University of Minnesota, 116 Church Street S.E., Minneapolis 55455, USA.

†Present address: Laboratoire d'Analyse et d'Architecture des Systèmes, 7 Avenue du Colonel Roche, BP 54200 31031, Toulouse, France.
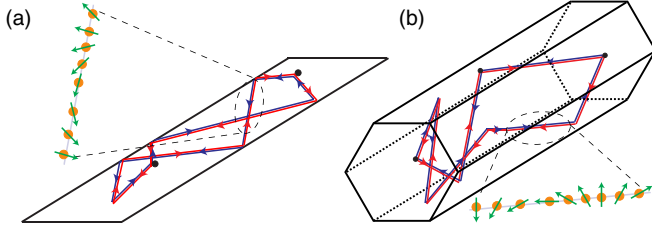
‡m.t.wimmer@tudelft.nl

FIG. 1. (Color online) Quantum interference along time-reversed paths in (a) 2D and (b) 3D nanowires. In both cases an inversion symmetry induces spin precession in between (boundary) scattering events.

The WAL correction to the classical conductivity can be computed in the quasiclassical theory as [25,29,30]

$$\Delta G = -\frac{e^2}{h}\frac{1}{L}\left[3\left(\frac{1}{l_\varphi^2}+\frac{4}{3l_{\rm so}^2}+\frac{1}{l_B^2}\right)^{-\frac{1}{2}}-\left(\frac{1}{l_\varphi^2}+\frac{1}{l_B^2}\right)^{-\frac{1}{2}}\right.$$
$$\left.-3\left(\frac{1}{l_\varphi^2}+\frac{4}{3l_{\rm so}^2}+\frac{d}{l_e^2}+\frac{1}{l_B^2}\right)^{-\frac{1}{2}}+\left(\frac{1}{l_\varphi^2}+\frac{d}{l_e^2}+\frac{1}{l_B^2}\right)^{-\frac{1}{2}}\right]. \tag{1}$$

The length scales in this expression are the nanowire length L, the mean free path l_e, the phase coherence length l_φ, the magnetic dephasing length l_B, and the spin relaxation length $l_{\rm so}$. The mean free path $l_e = v_F\tau_e$, where τ_e is the mean time between scattering events and v_F the Fermi velocity. In addition, the remaining length scales are also related to corresponding time scales as

$$l_{B,\varphi,{\rm so}} = \sqrt{D\tau_{B,\varphi,{\rm so}}}, \tag{2}$$

where $D = \frac{1}{d}v_F l_e$ the diffusion constant in d dimensions ($d = 3$ for bottom-up grown nanowires).

In the quasiclassical theory, τ_φ (and hence l_φ) is a phenomenological parameter. In contrast, τ_B and $\tau_{\rm so}$ are computed from a microscopic Hamiltonian, by averaging the quantum mechanical propagator over classical trajectories (a summary of the quasiclassical theory is given in the Supplemental Material [31]). τ_B and $\tau_{\rm so}$ thus depend not only on microscopic parameters (magnetic field B and SOI strength, respectively), but through the average over trajectories also on dimensionality, confinement, and l_e. We focus on the case where Rashba SOI due to an effective electric field in the z direction, perpendicular to the wire and substrate, dominates. Then the microscopic SOI Hamiltonian is $\frac{\alpha_R}{\hbar}(p_x\sigma_y - p_y\sigma_x)$, where $\sigma_{x,y}$ are Pauli matrices and $p_{x,y}$ the momentum operators. The corresponding spin-orbit precession length l_R equals $\hbar^2/m^*\alpha_R$. In our treatment we neglect the Zeeman splitting E_Z since we concentrate on the regime of large Fermi wave vector k_F such that $\alpha_R k_F \gg E_Z$.

The quasiclassical description is valid if the Fermi wavelength $\lambda_F \ll l_e, l_R$, and much smaller than the transverse extent W of the nanowire, i.e., for many occupied subbands. In particular, the quasiclassical method remains valid even if $l_R < l_e, W$ [32]. Additional requirements are given in Ref. [31].

We evaluate τ_B and $\tau_{\rm so}$ numerically by averaging over random classical paths for a given nanowire geometry. The paths consist of piecewise linear segments of freely moving
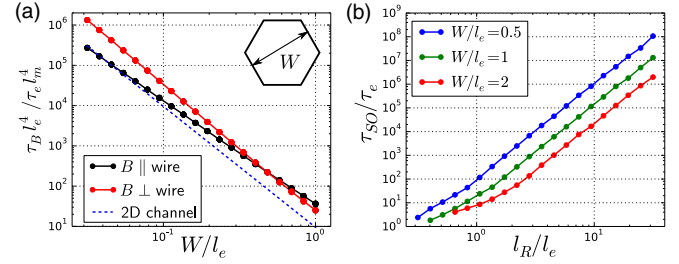

FIG. 2. (Color online) (a) Normalized dephasing time $\tau_B l_e^4/\tau_e l_m^4$ as a function of W/l_e for a hexagonal nanowire (see inset) for fields parallel (black) and perpendicular (red) to the nanowire. Dots are numerical data for different l_m in the range 1–$10^{2.5}$ (10–20 points per W), and solid lines are a fit to Eq. (3). The dashed line is the 2D wire result of [25]. (b) $\tau_{\rm so}/\tau_e$ as a function of spin-orbit strength l_R/l_e and different wire diameters in a 3D hexagonal nanowire.

electrons with constant speed [29,33], only scattered randomly from impurities and specularly at the boundary (for numerical details, see Ref. [31]). These assumptions imply a uniform electron density in the nanowire. Specular boundary reflection is expected as our wires have no surface roughness [34].

We apply our theory to nanowires with a hexagonal cross section and diameter W [see the inset in Fig. 2(a)] in the quasiballistic regime $l_e \gtrsim W$. Figure 2(a) shows the magnetic dephasing time τ_B (normalized by $\tau_e l_m^4/l_e^4$ with $l_m = \sqrt{\hbar/eB}$) as a function of wire diameter. Both parallel and perpendicular fields give rise to magnetic dephasing due to the three dimensionality of the electron paths, in contrast to two-dimensional systems where only a perpendicular field is relevant (see Fig. 1). The different field directions show a different dependence on W, with, remarkably, τ_B (and thus l_B) independent of field orientation for $W/l_e = 0.5$. Our results for $\tau_{\rm so}$ as a function of l_R are shown in Fig. 2(b). We find an increase of $\tau_{\rm so}$ as the wire diameter W is decreased, indicating that confinement leads to increased spin relaxation times.

For $l_{m,R}, l_e \gtrsim W$ we can fit our results reliably as

$$\tau_{B,{\rm so}} = C\frac{l_{m,R}^4}{W^\gamma l_e^{(4-\gamma)}}. \tag{3}$$

This is shown for τ_B in Fig. 2(a), where data for different l_m and W collapse to one line. In particular, for τ_B, we find $C = 34.1 \pm 0.1$ and $\gamma = 2.590 \pm 0.002$ for the parallel field, and $C = 22.3 \pm 0.3$ and $\gamma = 3.174 \pm 0.003$ for the perpendicular field. For $\tau_{\rm so}$ we find $C = 8.7 \pm 0.5$ and $\gamma = 3.2 \pm 0.1$. Note that our numerics is valid beyond the range where the fit (3) is applicable. For example, for $l_R \lesssim W$, the numerical result deviates from the power law of (3) as seen in Fig. 2(b); in this regime only the numerical result can be used.

The fit (3) allows for a quantitative comparison of our 3D wire results to 2D wires: Both are similar in that there is flux cancellation ($\gamma > 2$) [25] and suppressed spin relaxation due to confinement. However, they exhibit a significantly different power law. As an example, in Fig. 2(a) we compare to the 2D wire result for weak fields from Ref. [25] ($C = 10.8$, $\gamma = 3$) that can differ by an order of magnitude from our results. This emphasizes the need for an accurate description of geometry for a quantitative analysis of WAL.
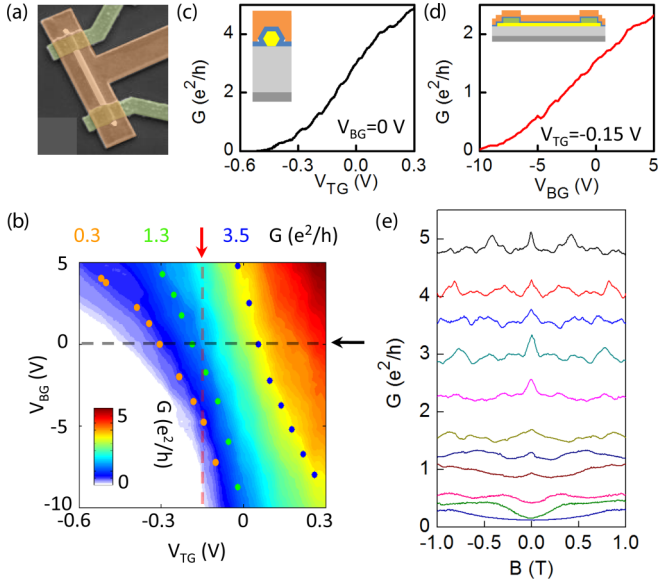
FIG. 3. (Color online) (a) False color scanning electron microscopy image of device I. The contact spacing is $2\,\mu m$. Device fabrication is described in Ref. [31]. (b) Conductance G as a function of top-gate voltage V_{TG} and back-gate voltage V_{BG}. Arrows and dashed lines indicate cross sections shown in (c) and (d). Dots indicate voltages (V_{BG}, V_{TG}) at which traces in Fig. 4(a) were taken (the same dot color corresponds to the same G). Data taken with a 10 mV voltage bias at a temperature of 4.2 K. (c) G as a function of V_{TG} at $V_{BG} = 0$ V. Inset: Radial cross section of the device. The blue layer is HfO$_2$. (d) G as a function of V_{BG} at $V_{TG} = -0.15$ V. Inset: Axial cross section of the device. (e) Conductance, as a function of magnetic field, at several values of device conductance controlled by V_{TG}, $V_{BG} = 0$ V. Data taken with ac excitation $V_{ac} = 100\,\mu V_{rms}$.

FIG. 4. (Color online) (a) Magnetoconductance (MC) obtained after averaging MC traces taken at the same G. For $G = 3.5, 1.3$, and $0.3e^2/h$ the voltages at which these MC traces were taken are indicated in Fig. 3(b). Averaged MC traces have been centered to $\Delta G = 0$ at $B = 0$ T. $G(B = 1$ T) is indicated on the right. Red curves are fits to the data assuming $\frac{l_e}{W} = 1$. (b) Spin relaxation length l_{so} obtained from the fits of (a) ($\frac{l_e}{W} = 1$, blue points) and obtained from fits with $\frac{l_e}{W} = 2$ (red points). Standard deviation of the fit outcomes is indicated. The distribution around the blue and red points (green and gray bands, respectively) is given by the spin-orbit lengths obtained from fits with an effective width 15 nm smaller (resulting in longer l_{so}) or larger (resulting in shorter l_{so}) than the expected wire width $W = 90$ nm. (c) Phase coherence length l_φ and (d) spin precession length l_R as a function of device conductance. Figure formatting is as in (b).

We continue with the experiment. InSb nanowires [35] with diameter $W \approx 100$ nm are deposited onto a substrate with a global back gate. A large ($\geqslant 2\,\mu m$) contact separation ensures sufficient scattering between the source and drain. After contact deposition a HfO$_2$ dielectric layer is deposited and the device is then covered by metal, creating an Ω-shaped top gate [Fig. 3(a) and the insets of Figs. 3(c) and 3(d)]. Nanowire conductance is controlled with the top- and back-gate voltage, reaching a conductance up to $\sim 5e^2/h$ [Fig. 3(b)]. The device design leads to a strong top-gate coupling [Fig. 3(c)], while back gate coupling is weaker [Fig. 3(d)]. From a field-effect mobility of $\sim 11\,000$ cm^2/V s a ratio of the mean free path to the wire diameter $l_e/W = 1$–2 is estimated [31,36].

At large G the magnetoconductance, measured with conductance controlled by the top gate at a temperature $T = 4.2$ K and with B perpendicular to the nanowire and substrate plane, shows an increase of conductance of ~ 0.2 to $\sim 0.3e^2/h$ around $B = 0$ [Fig. 3(e)]. $G(B)$ is, apart from reproducible conductance fluctuations, flat at $B > 200$ mT, which is further evidence of specular boundary scattering [33]. On reducing conductance below $\sim 1.5e^2/h$, WAL becomes less pronounced and a crossover to weak localization (WL) is seen.

Reproducible conductance fluctuations, most clearly seen at larger B [Fig. 3(e)], affect the WAL peak shape. To suppress these fluctuations, several (7–11) MC traces are taken at the same device conductance [see Fig. 3(b)]. After averaging
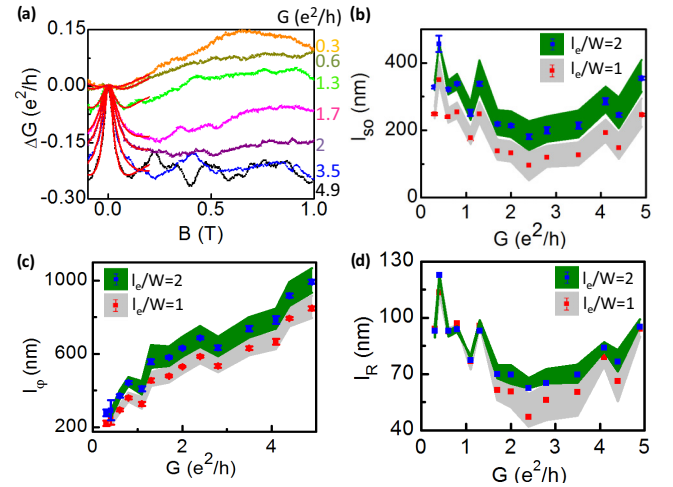
these traces, WAL remains while the conductance fluctuations are greatly suppressed [Fig. 4(a)]. Also here on reduction of conductance, a crossover from WAL to WL is seen. Very similar results are obtained when averaging MC traces obtained as a function of top-gate voltage with $V_{BG} = 0$ V [31]. We expect that several (~ 10) subbands are occupied at a device conductance $G \gtrsim 2e^2/h$ (see Ref. [31]). Hence, our quasiclassical approach is valid and we fit the averaged MC traces to Eq. (1) with l_{so}, l_φ and the conductance at a large magnetic field $\Delta G(B \to \infty)$ as fit parameters. l_B is extracted from Eq. (3). The wire diameter and mean free path are fixed in each fit, but we extract fit results for a wire diameter deviating from its expected value and for both $\frac{l_e}{W} = 1$ and $\frac{l_e}{W} = 2$. We find good agreement between data and fits [see Fig. 4(a)]. While showing fit results covering the full range of G, we base our conclusions on results obtained in the quasiclassical transport regime $G \gtrsim 2e^2/h$.

On increasing conductance, the spin relaxation length first decreases to $l_{so} \approx 100$–200 nm, and then increases again to $l_{so} \approx 200$–400 nm when $G \geqslant 2.5e^2/h$ [Fig. 4(b)]. The phase coherence length [Fig. 4(c)] shows a monotonous increase with device conductance. This increase can be explained by the density dependence of either the diffusion constant or the electron-electron interaction strength [37], often reported as the dominant source of dephasing in nanowires [11,38].

Spin relaxation [39] in our device can possibly occur via the Elliot-Yafet [40] or the D'yakonov-Perel' mechanism [41],
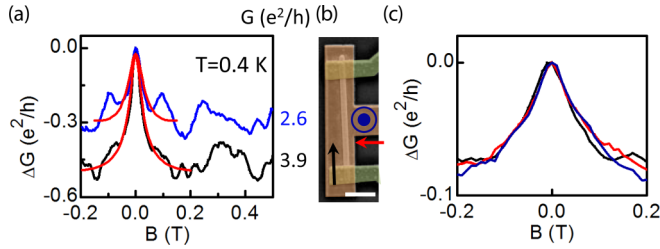
FIG. 5. (Color online) (a) Magnetoconductance (MC) at $T = 0.4$ K. Each MC trace is obtained after averaging 21 MC traces taken along the top-gate controlled pinch-off trace shown in Fig. 3(c) ($V_{BG} = 0$ V). The black (blue) trace is the average of traces taken between $V_{TG} = 0.34$ V and $V_{TG} = 0.14$ V ($V_{TG} = 0.12$ V and $V_{TG} = -0.08$ V) with steps of 20 mV. The voltage excitation V_{ac} was $10\,\mu V_{rms}$. $G(B = 0.5$ T) is indicated on the right. Phase coherence and spin relaxation length obtained from fits (in red) to the traces is 1078 ± 32 (1174 ± 39) nm and of 95 ± 18 (205 ± 16) nm, respectively, for $\frac{l_e}{W} = 1$ (2). Values obtained at $G = 2.6e^2/h$ are given in Ref. [31]. (b) False color scanning electron microscope image of device II with different magnetic field orientations indicated by the arrows. The scale bar is $1\,\mu$m. (c) MC obtained with B parallel to the nanowire (in-plane angle with respect to the nanowire $\theta \approx 5°$, black), B perpendicular to the nanowire in the plane of the substrate ($\theta \approx 95°$, red), and B perpendicular to the substrate plane (blue). $V_{TG} = 0.2$ V, $V_{BG} = 0$ V. Smaller ΔG compared to the preceding data is due to a larger contact resistance (~ 10 kΩ) of this device for which no correction was made.

corresponding to spin randomization at or in between scattering events, respectively. The Elliot-Yafet contribution can be estimated as $l_{so,EY} = \sqrt{\frac{3}{8}\frac{E_G}{E_F}l_e\frac{(E_G+\Delta_{so})(3E_G+2\Delta_{so})}{\Delta_{so}(2E_G+\Delta_{so})}} \gtrsim$ 300–600 nm [42], with band gap $E_G = 0.24$ eV, Fermi energy $E_F \leqslant 100$ meV, spin-orbit gap $\Delta_{so} = 0.8$ eV, and $\frac{l_e}{W} = 1$–2. For the D'yakonov-Perel' mechanism, we note that our nanowires have a zinc-blende crystal structure, grown in the [111] direction, where the Dresselhaus SOI is absent for momentum along the nanowire [43]. We therefore expect that the Rashba SOI is the dominant source of spin relaxation, in agreement with previous experiments [15]. As found in our theoretical analysis, it is then crucial to capture confinement effects accurately. Our l_{so} correspond to $\frac{\tau_{so}}{\tau_e} = 2$ –15 that are captured well by our simulations [44]. Given that $W \approx l_R$, we extract the l_R corresponding to our $\frac{\tau_{so}}{\tau_e}$ directly from Fig. 2(b). We extract spin precession lengths l_R of 50–100 nm, shown in Fig. 4(d), corresponding to $\alpha_R = 0.5$–1.0 eV Å. MC measurements on a second device show very similar l_R [31].

To confirm the interpretation of our MC measurements we extract MC at a lower temperature $T = 0.4$ K [Fig. 5(a)]. We find larger WAL amplitudes of up to $\Delta G \sim 0.5e^2/h$, while the width of the WAL peak remains approximately the same as at $T = 4.2$ K, corresponding to a longer l_φ at lower temperature, with approximately constant l_{so}. A longer l_φ is expected at lower temperature, as the rate of inelastic scattering, responsible for the loss of phase coherence, is reduced in this regime.

Our theoretical analysis found similar dephasing times for magnetic fields perpendicular and parallel to the nanowire for our estimated mean free paths, $l_e/W = 1$–2. Indeed, we observe virtually identical WAL for fields parallel and perpendicular to the nanowire in our second device [see Figs. 5(b) and 5(c)]. WAL in the first device is also very similar for both field directions [31]. This is in striking contrast to MC measurements in two-dimensional systems where only a perpendicular magnetic field gives strong dephasing due to orbital effects. It also provides strong support for the assumptions made in our theory, and emphasizes the importance of including the three-dimensional nature of nanowires to understand their MC properties. In contrast, WL is anisotropic [31], which we attribute to a different density distribution at low conductance compared to the high conductance at which WAL is seen.

Relevant to Majorana fermion experiments is the spin-orbit energy $E_{SO} = \frac{m\alpha_R^2}{2\hbar^2}$, which is 0.25–1 meV in our devices. These values compare favorably to InAs nanowires that yield $\alpha_R^{InAs} = 0.1$–0.3 eV Å [38,45] and corresponding $E_{SO}^{InAs} = 15$–135 μeV. E_{SO}^{InSb} is similar or slightly larger than the reported spin-orbit energies in Ge/Si core-shell nanowires ($E_{SO}^{Ge/Si} = 90$–600 μeV [46]), while α_R^{InSb} is larger than $\alpha_R^{Ge/Si} = 0.07$–0.18 eV Å). Note that the device geometries and expressions for $\alpha_R(l_{so})$ used by different authors vary and that often only l_{so}, not l_R, is evaluated. With our E_{SO} we then find, following the analysis of Ref. [4], a topological gap of ~ 0.1–1 K [31] even for our moderate mobilities of order $10\,000$ cm^2/V s. This gap largely exceeds the temperature and previous estimates. Hence, our findings underline the potential of InSb nanowires in the study of Majorana fermions.

[1] J. Alicea, Rep. Prog. Phys. **75**, 076501 (2012).

[2] Y. Oreg, G. Refael, and F. von Oppen, Phys. Rev. Lett. **105**, 177002 (2010).

[3] R. M. Lutchyn, J. D. Sau, and S. Das Sarma, Phys. Rev. Lett. **105**, 077001 (2010).

[4] J. D. Sau, S. Tewari, and S. Das Sarma, Phys. Rev. B **85**, 064512 (2012).

[5] R. Winkler, *Spin-Orbit Coupling Effects in Two-Dimensional Electron and Hole Systems* (Springer, Berlin, 2003).

[6] J. Fabian, A. Matos-Abiague, C. Ertler, P. Stano, and I. Zutic, Acta Phys. Slovaca **57**, 565 (2007).

[7] V. Mourik, K. Zuo, S. M. Frolov, S. R. Plissard, E. P. A. M. Bakkers, and L. P. Kouwenhoven, Science **336**, 1003 (2012).

[8] A. Das, Y. Ronen, Y. Most, Y. Oreg, M. Heiblum, and H. Shtrikman, Nat. Phys. **8**, 887 (2012).

[9] M. T. Deng, C. L. Yu, G. Y. Huang, M. Larsson, P. Caroff, and H. Q. Xu, Nano Lett. **12**, 6414 (2012).

[10] H. O. H. Churchill, V. Fatemi, K. Grove-Rasmussen, M. T. Deng, P. Caroff, H. Q. Xu, and C. M. Marcus, Phys. Rev. B **87**, 241401(R) (2013).

[11] R. L. Kallaher, J. J. Heremans, N. Goel, S. J. Chung, and M. B. Santos, Phys. Rev. B **81**, 035335 (2010).

[12] R. L. Kallaher, J. J. Heremans, N. Goel, S. J. Chung, and M. B. Santos, Phys. Rev. B **81**, 075303 (2010).

[13] E. I. Rashba, Sov. Phys. Solid State **2**, 1109 (1960).

[14] H. A. Nilsson, P. Caroff, C. Thelander, M. Larsson, J. B. Wagner, L.-E. Wernersson, L. Samuelson, and H. Q. Xu, Nano Lett. **9**, 3151 (2009).

[15] S. Nadj-Perge, V. S. Pribiag, J. W. G. van den Berg, K. Zuo, S. R. Plissard, E. P. A. M. Bakkers, S. M. Frolov, and L. P. Kouwenhoven, Phys. Rev. Lett. **108**, 166801 (2012).

[16] M. Wimmer, A. R. Akhmerov, J. P. Dahlhaus, and C. W. J. Beenakker, New J. Phys. **13**, 053016 (2011).

[17] M. Houzet, J. S. Meyer, D. M. Badiane, and L. I. Glazman, Phys. Rev. Lett. **111**, 046401 (2013).

[18] T. Hyart, B. van Heck, I. C. Fulga, M. Burrello, A. R. Akhmerov, and C. W. J. Beenakker, Phys. Rev. B **88**, 035121 (2013).

[19] J. Nitta, T. Akazaki, H. Takayanagi, and T. Enoki, Phys. Rev. Lett. **78**, 1335 (1997).

[20] G. Engels, J. Lange, T. Schäpers, and H. Lüth, Phys. Rev. B **55**, R1958 (1997).

[21] S. Hikami, A. I. Larkin, and Y. Nagaoka, Progr. Theor. Phys. **63**, 707 (1980).

[22] S. V. Iordanskii, Yu. B. Lyanda-Geller, and G. E. Pikus, JETP Lett. **60**, 206 (1994).

[23] G. Bergmann, Phys. Rep. **107**, 1 (1984).

[24] B. L. Al'tshuler, A. G. Aronov, A. I. Larkin, and D. E. Khmel'nitskii, Sov. Phys. JETP **54**, 411 (1981).

[25] C. W. J. Beenakker and H. van Houten, Phys. Rev. B. **38**, 3232 (1988).

[26] S. Kettemann, Phys. Rev. Lett. **98**, 176808 (2007).

[27] A. A. Kiselev and K. W. Kim, Phys. Rev. B **61**, 13115 (2000).

[28] Th. Schäpers, V. A. Guzenko, M. G. Pala, U. Zülicke, M. Governale, J. Knobbe, and H. Hardtdegen, Phys. Rev. B **74**, 081301(R) (2006).

[29] S. Chakravarty and A. Schmid, Phys. Rep. **140**, 193 (1986).

[30] C. Kurdak, A. M. Chang, A. Chin, and T. Y. Chang, Phys. Rev. B **46**, 6846 (1992).

[31] See Supplemental Material at http://link.aps.org/supplemental/10.1103/PhysRevB.91.201413 for details of the numerical simulations and additional experimental data.

[32] O. Zaitsev, D. Frustaglia, and K. Richter, Phys. Rev. B **72**, 155325 (2005).

[33] C. W. J. Beenakker and H. van Houten, Solid State Phys. **44**, 1 (1991).

[34] T. Xu, K. A. Dick, S. Plissard, T. H. Nguyen, Y. Makoudi, M. Berthe, J.-P. Nys, X. Wallart, B. Grandidier, and P. Caroff, Nanotechnology **23**, 095702 (2012). We extrapolate the results on InAsSb wires to InSb since the flatness of the facets results from the introduction of Sb.

[35] S. R. Plissard, D. R. Slapak, M. A. Verheijen, M. Hocevar, G. W. G. Immink, I. van Weperen, S. Nadj-Perge, S. M. Frolov, L. P. Kouwenhoven, and E. P. A. M. Bakkers, Nano Lett. **12**, 1794 (2012).

[36] S. R. Plissard, I. van Weperen, D. Car, M. A. Verheijen, G. W. G. Immink, J. Kammhuber, L. J. Cornelissen, D. B. Szombati, A. Geresdi, S. M. Frolov, L. P. Kouwenhoven, and E. P. A. M. Bakkers, Nat. Nanotechnol. **8**, 859 (2013).

[37] J. J. Lin and J. P. Bird, J. Phys.: Condens. Matter **14**, R501 (2002).

[38] D. Liang and X. P. A. Gao, Nano Lett. **12**, 3263 (2012).

[39] M. W. Wu, J. H. Jiang, and M. Q. Weng, Phys. Rep. **493**, 61 (2010).

[40] Y. Yafet, *Solid State Physics* (Academic, New York, 1963), Vol. 14; R. J. Elliott, Phys. Rev. **96**, 266 (1954).

[41] M. I. D'yakonov and V. I. Perel', Sov. Phys. Solid State **13**, 3023 (1972).

[42] J. Chazalviel, Phys. Rev. B **11**, 1555 (1975).

[43] Furthermore, even for [100] nanowires, the Dresselhaus SOI is weak: In this case the maximum linear Dresselhaus SOI strength is γk_F^2 (with γ the cubic Dresselhaus SOI strength), yielding a spin-orbit length $l_D = \hbar^2/m^*\gamma k_F^2$. With $\gamma = 437$ eV $\mathring{A}^3$ [6] and $E_F \leqslant 100$ meV we estimate $l_D > 300$ nm.

[44] Exceptions are the smallest values of l_{so} at $G = 2.4$ and $2.8e^2/h$: When assuming a wire width larger than the expected value ($W = 105$ nm) we find $\frac{\tau_{so}}{\tau_e} \sim 1$. In this case the l_R corresponding to the lowest simulated value of $\frac{\tau_{so}}{\tau_e}$ has been chosen as a lower bound.

[45] A. E. Hansen, M. T. Björk, I. C. Fasth, C. Thelander, and L. Samuelson, Phys. Rev. B **71**, 205328 (2005); P. Roulleau, T. Choi, S. Riedi, T. Heinzel, I. Shorubalko, T. Ihn, and K. Ensslin, *ibid.* **81**, 155449 (2010); S. Dhara, H. S. Solanki, V. Singh, A. Narayanan, P. Chaudhari, M. Gokhale, A. Bhattacharya, and M. M. Deshmukh, *ibid.* **79**, 121311(R) (2009); S. Estévez Hernández, M. Akabori, K. Sladek, C. Volk, S. Alagha, H. Hardtdegen, M. G. Pala, N. Demarina, D. Grützmacher, and T. Schäpers, *ibid.* **82**, 235303 (2010).

[46] X.-J. Hao, T. Tu, G. Cao, C. Zhou, H.-O. Li, G.-C. Guo, W. Y. Fung, Z. Ji, G.-P. Guo, and W. Lu, Nano Lett. **10**, 2956 (2010); A. P. Higginbotham, F. Kuemmeth, T. W. Larsen, M. Fitzpatrick, J. Yao, H. Yan, C. M. Lieber, and C. M. Marcus, Phys. Rev. Lett. **112**, 216806 (2014).